RSC Advances

PAPER

View Article Online
View Journal | View Issue

Check for updates

Cite this: *RSC Adv.*, 2025, **15**, 29300

Comparison of the efficacy of FITC-conjugated dextran, PEG, and HA as intraoperative navigation materials in pancreatic cancer

Xiao Zhou,[a] Huali Huang,[b] Lifeng Luo,[c] Chenxi Cui[c] and Hongmian Jiang *[c]

Pancreatic cancer, a highly aggressive solid tumor, presents multiple challenges in treatment. Although surgical resection is the primary treatment for early-stage non-metastatic cases, the deep abdominal location of the pancreas complicates precise intraoperative localization, adversely affecting surgical outcomes and patient prognosis. To address these clinical challenges, we aim to develop an innovative intraoperative navigation platform for precision tumor-targeted delivery. We systematically evaluated the tumor-targeting specificity and tissue-penetrating capacity of three hydrosoluble polymers, *i.e.*, dextran, PEG, and HA, in pancreatic carcinoma models. The uptake kinetics of these materials in cancer cells and their penetration dynamics across complex tumor matrices were quantitatively evaluated *via in vitro* assays and three-dimensional tumor spheroid models. Complementary *in vivo* validation involved the use of PNAC-1 cell subcutaneous xenograft models to map the spatiotemporal distribution and tumoral accumulation of the lead candidates. Results demonstrated that dextran-FITC had a superior tumor-targeting performance, showing a significantly higher fluorescence intensity than PEG-FITC and HA-FITC. These preliminary data reveal significant heterogeneity in the intertumoral localization efficiency among the polymer carriers, establishing a mechanistic foundation for intraoperative navigation. Through rational optimization of carrier selection and delivery modalities, this platform aims to enhance surgical precision, minimize off-target effects, and ultimately improve clinical outcomes.

Received 31st March 2025
Accepted 1st August 2025

DOI: 10.1039/d5ra02236c

rsc.li/rsc-advances

Open Access Article. Published on 19 August 2025. Downloaded on 5/22/2026 2:24:16 AM.
This article is licensed under a Creative Commons Attribution-NonCommercial 3.0 Unported Licence.

1 Introduction

Solid tumors constitute approximately 80% of all malignant tumors and are primarily characterized by the formation of space-occupying lesions.[1] Advances in imaging technologies now allow the detection of many solid tumors at early stages.[2] Surgical resection of non-metastatic primary tumors theoretically enables clinical cure.[3] However, in clinical practice, tumors located in the abdominal or thoracic cavities often pose significant challenges to surgical excision, including poorly defined margins and the presence of satellite lesions, which may compromise surgical precision.[4,5]

Pancreatic cancer is one of the most aggressive and lethal tumors worldwide, with a five-year survival rate that remains exceedingly low and limited treatment options available.[6] In clinical practice, computed tomography (CT) serves as the first-line imaging modality for pancreatic ductal adenocarcinoma (PDAC), enabling the detection of tumors <20 mm in diameter, which facilitates early diagnosis.[7] This critical window establishes patient eligibility for surgical intervention, which remains the first-line treatment for pancreatic cancer. However, the deep-seated anatomical location of pancreatic tumors within the retroperitoneum frequently creates intraoperative challenges such as suboptimal tumor localization and satellite lesions. Furthermore, the development of modified radical surgery has led to a shift in the extent of resection from organ removal toward excising lesions with limited margins, aiming to maximally preserve organ integrity and improve patients' postoperative quality of life.[8,9] The application of intraoperative localization methods can significantly enhance surgical precision by effectively locating lesions and clarifying the surgical scope.[10] Ultrasound is currently the most widely employed intraoperative diagnostic tool; however, it has limitations, including poor localization accuracy for deep lesions, suboptimal visualization in obese patients, and potential interference from gas or fluid, which may degrade the image quality.[11,12] Therefore, combining complementary real-time tumor localization systems may be more beneficial for improving the accuracy of intraoperative positioning.

Intraoperative navigation systems employ targeted tracing technologies (such as fluorescence imaging) to label specific targeting systems with tracing molecules, achieving precise tumor targeting. During surgery, these systems enable real-time visualization of the tumor location, assisting surgeons in

[a]*Department of Breast Surgery, Guangxi Medical University Cancer Hospital, China*
[b]*Department of Gastroenterology, The Fifth Affiliated Hospital of Guangxi Medical University, China*
[c]*Department of Pathology, The Fifth Affiliated Hospital of Guangxi Medical University, China. E-mail: JHMMED@126.com*

© 2025 The Author(s). Published by the Royal Society of Chemistry

Open Access Article. Published on 19 August 2025. Downloaded on 5/22/2026 2:24:16 AM.
This article is licensed under a Creative Commons Attribution-NonCommercial 3.0 Unported Licence.

precise tumor resection under visual guidance. This technology not only enhances the tumor removal precision and minimizes collateral damage to surrounding healthy tissue, but also dynamically monitors biological events (*e.g.*, probe distribution and cellular responses) during surgery, improving intraoperative decision-making.[13] The high resolution and specificity of targeted fluorescence imaging establish it as a valuable tool for tumor localization, significantly enhancing surgical precision and operative success, which critically improves patient outcomes.[14] Recently, researchers have increasingly focused on the potential of macromolecular materials for tumor probe delivery. Polymers such as dextran, polyethylene glycol (PEG), and hyaluronic acid (HA) exhibit favorable biocompatibility and targeting properties in probe delivery systems.[15] Chemical modification renders these materials non-toxic, while enhancing the accumulation of the probe within tumor tissues, thereby offering new approaches for surgical navigation.[16]

Dextran, a natural polysaccharide, is extensively utilized in nanomedicine as a probe carrier owing to its water solubility, low toxicity, and biodegradability.[17] Upon chemical modification, dextran forms stable complexes with cancer probes, augmenting their tumor tissue accumulation and penetration.[18] Notably, dextran nanoparticles can breach stromal barriers in pancreatic cancer, dramatically improving the penetration and retention of the probe.[19] Polyethylene glycol (PEG), known for its "stealth" properties, diminishes immune-mediated clearance and extends the systemic circulation time, leading to enhanced tumor-specific accumulation.[20] PEGylation significantly improves the targeting and stability of nanocarriers (*e.g.*, liposomes), while mitigating systemic toxicity.[21] Critically, PEG-modified targeting agents show significant promise for applications in pancreatic cancer.[22] Hyaluronic acid (HA), a glycosaminoglycan ubiquitous in the extracellular matrix, achieves selective targeting of pancreatic cancer cells by binding to over-expressed CD44 receptors.[23] This targeting mechanism establishes HA as a pivotal carrier material for pancreatic cancer therapy.[24] Previous studies have indicated that HA-conjugated nanoprobe carriers exhibit enhanced accumulation within solid tumors, improving their penetration and imaging output within the tumor microenvironment.[25] Collectively, these foundational findings validate the translational potential of these polymeric materials as nanoprobe delivery platforms for tumor-targeting applications.

This study aims to compare the performance of dextran, PEG, and HA as nanocarriers for tumor-targeted tracer delivery in pancreatic cancer models. To enable *in vivo* tracking capability, all three carriers were labeled with fluorescein isothiocyanate (FITC), allowing the real-time monitoring of their distribution and accumulation in pancreatic tumors. By utilizing fluorescence imaging to track the carrier distribution in tumor tissues, we intend to achieve precise intraoperative tumor localization. Furthermore, we evaluate the potential toxicity of these carriers, establishing a preclinical foundation for their clinical translation. This integrated approach aims to pioneer innovative strategies for intraoperative navigation and positioning systems in pancreatic cancer, potentially enhancing the surgical precision (Scheme 1).

2 Materials and methods

2.1. Experimental materials

All reagents used were of analytical grade and employed without further purification. Ethanol, dimethyl sulfoxide (DMSO), and

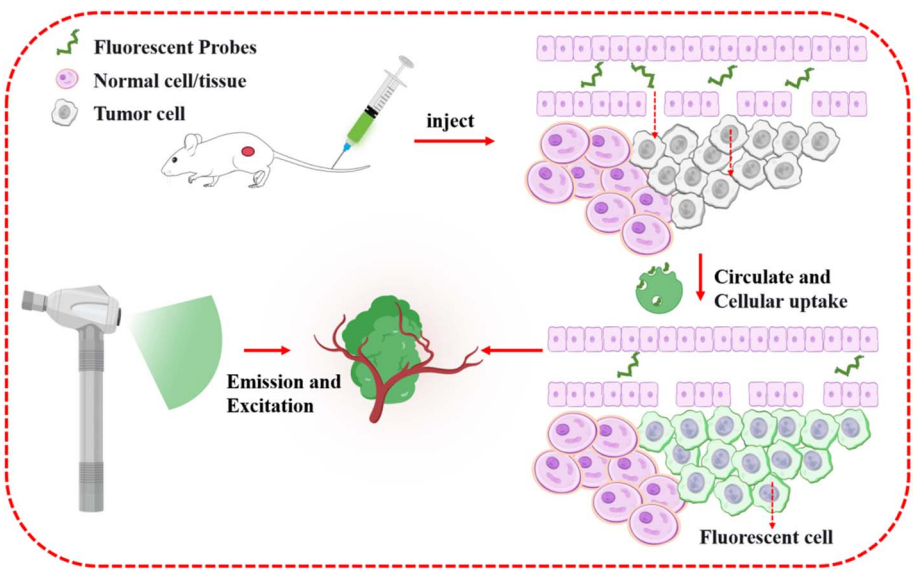

Scheme 1 Tumor targeting and visualization of fluorescent molecules in mice. First, fluorescently labeled molecules (such as dextran-FITC, PEG-FITC, and HA-FITC) are injected intravenously into mice, allowing them to circulate throughout the body of the mice. Through the enhanced permeability and retention (EPR) effect, the fluorescent molecules preferentially accumulate in the tumor tissue, utilizing the high permeability and low lymphatic drainage characteristics of the tumor vasculature to enter the tumor area. Subsequently, the fluorescent molecules penetrate further into the deeper layers of the tumor tissue. Finally, by using imaging equipment with specific excitation and emission wavelengths, the fluorescent molecules are excited, enabling the visualization of the tumor tissue. This allows a clear delineation of tumor boundaries and internal structure, facilitating precise intraoperative guidance and tumor mapping.

© 2025 The Author(s). Published by the Royal Society of Chemistry

Open Access Article. Published on 19 August 2025. Downloaded on 5/22/2026 2:24:16 AM. This article is licensed under a Creative Commons Attribution-NonCommercial 3.0 Unported Licence.

sodium bicarbonate ($NaHCO_3$) were obtained from JSK Biotechnology (Shanghai, China). Dextran (1 kDa) was purchased from Aladdin Biochemical Technology (Shanghai, China); PEG-NH_2 (1 kDa) from Ruixi Biotechnology (Shanxi, Xian, China); and HA-NH_2 (1 kDa) from Shenzhen MeloPEG Biotechnology (Guangdong, Shenzhen, China). Fluorescein isothiocyanate (FITC) was supplied by Aladdin Biochemical Technology (Shanghai, China). The Cell Counting Kit-8 (CCK-8) was obtained from Beyotime Biotechnology (Shanghai, China). Corning® Matrigel® Basement Membrane Matrix (354234) was sourced from Corning Inc. (New York, USA). The human pancreatic cancer cell line (PNAC-1) was purchased from GeneBio Biotech (Guangdong, Guangzhou, China).

2.2. Characterization

^{1}H NMR spectra were recorded on a 600 MHz NMR spectrometer (Bruker AVANCE NEO). Fluorescence images were captured using an inverted fluorescence microscope (Nikon, NIS-Elements software). UV and fluorescence emission spectra were measured with a SpectraMax i3x microplate reader (Molecular Devices). *In vivo* imaging was conducted using a small animal optical imaging system (AniView100, BioLight Technology). Grayscale values were quantified using the ImageJ software.

2.3. Synthesis

2.3.1 Synthesis of FITC-labeled dextran (dextran-FITC). The synthesis of the tumor-targeted fluorescent material dextran-FITC is illustrated in Fig. 1A. The detailed experimental procedures follow prior reports.[26] Briefly, dextran (543 mg) was dissolved in 10 mL of DMSO and stirred until fully dissolved. The pH was adjusted to 9.5 with 0.5 mol mL^{-1} $NaHCO_3$, and FITC (25 mg) was added. The reaction mixture was stirred for 6 h at room temperature in the dark. Anhydrous ethanol was added to the filtrate until reaching 80% (v/v), resulting in a precipitate, which was centrifuged, and the supernatant was discarded. The precipitate was redissolved in water and precipitated with ethanol three times. Finally, it was washed with anhydrous ethanol until no fluorescence was detected in the supernatant. The sample was separated using a pre-equilibrated Sephadex G25 dextran gel column, with phosphate-buffered saline (PBS, pH 7.4) as the mobile phase. In this process, the large molecular target products are eluted first, followed by the small molecular impurities (such as unreacted FITC). Upon separation, 344 mg of dextran-FITC powder was obtained by freeze-drying. The molecular weight and chemical structure of the product were verified using ^{1}H NMR.

2.3.2 Synthesis of FITC-labeled PEG (PEG-FITC). The synthesis of the tumor-targeted fluorescent material PEG-FITC is shown in Fig. 1B. PEG-NH_2 (491 mg) was dissolved in 20 mL of water and added dropwise to 1 mg mL^{-1} FITC solution in DMSO. The sample was separated using a pre-equilibrated G25 dextran gel column, with a suitable buffer as the mobile phase. The large molecular target products were eluted preferentially, while the small molecular impurities (such as unreacted FITC) were eluted in the subsequent stages. After separation, PEG-FITC powder (211 mg) was obtained by freeze-drying, and the product was characterized by ^{1}H NMR.

2.3.3 Synthesis of FITC-labeled hyaluronic acid (HA-FITC). The synthesis of the tumor-targeted fluorescent material HA-FITC is shown in Fig. 1C. Activated HA-NH_2 (603 mg) was combined in 5 mL of distilled water, followed by the addition of FITC (50 mg). The reaction was stirred magnetically for 24 h. The sample was separated using a pre-equilibrated Sephadex G-25 column, employing PBS (pH = 7.4) as the mobile phase. During this process, the large molecular target products are eluted first, while small molecular impurities (such as unreacted FITC) are eluted afterward. After dialysis, the dialyzed mixture was irradiated under UV light to ensure the absence of free fluorescent molecules, and then freeze-dried for 48 h, yielding HA-FITC powder (319 mg).

2.3.4 GPC testing. The molecular weight of the fluorescently labeled polymer was determined using gel permeation chromatography (GPC). The experiment employed an Ultrahydrogel 250 column (250 Å, 6 μm, 7.8 mm × 300 mm, Waters). The mobile phase consisted of 20 mM phosphate buffer, with a flow rate of 1 mL min^{-1}, a column temperature of 40 °C, and an injection volume of 20 μL. A UV detector (480 nm) was used to measure the molecular weight, and a calibration curve was constructed using dextran standards.

2.3.5 Matrix-assisted laser desorption/ionization time-of-flight mass spectrometry (MALDI-TOF MS). Sample analysis was performed using matrix-assisted laser desorption time-of-flight mass spectrometry (MALDI-TOF MS). 2,5-Dihydroxybenzoic acid (DHB) was selected as the matrix at a concentration of 20 mg mL^{-1}. During sample preparation, DHB was dissolved in a suitable solvent (acetonitrile/water/trifluoroacetic acid, 50 : 49 : 1 v/v/v) to prepare a 20 mg mL^{-1} solution. This matrix solution was thoroughly mixed with the sample solution, spotted onto an MALDI target plate, and allowed to dry completely before loading the plate into the mass spectrometer. Analysis was conducted using a ultrafleXtreme™ MALDI-TOF mass spectrometer (Bruker Daltonics) operated in positive ion reflector mode. The laser source employed was an Nd:YAG laser (wavelength: 355 nm, frequency: 2 kHz) with the laser energy set at 90% of the maximum output and a pulse repetition rate of 1 kHz. Each sample spot accumulated 200 laser shots. Mass spectrometric data acquisition and processing were performed using the FlexImaging 3.0 software (Bruker Daltonics).

2.3.6 Fluorescence and UV-Vis spectral scanning. A measured volume of probe stock solution (10 mM) was transferred to a 1.5 mL centrifuge tube and diluted with PBS to achieve a final concentration of 10 μM. Following incubation at 37 °C for a specified duration, fluorescence and UV-Vis spectral data were acquired.

2.4. Cellular experiments

2.4.1 Cell culture. The PNAC-1 cell revival and culture protocol involved rapidly thawing frozen cells in a 37 °C water bath, centrifuging to remove the cryoprotectant, and seeding into

 © 2025 The Author(s). Published by the Royal Society of Chemistry

Open Access Article. Published on 19 August 2025. Downloaded on 5/22/2026 2:24:16 AM.
This article is licensed under a Creative Commons Attribution-NonCommercial 3.0 Unported Licence.

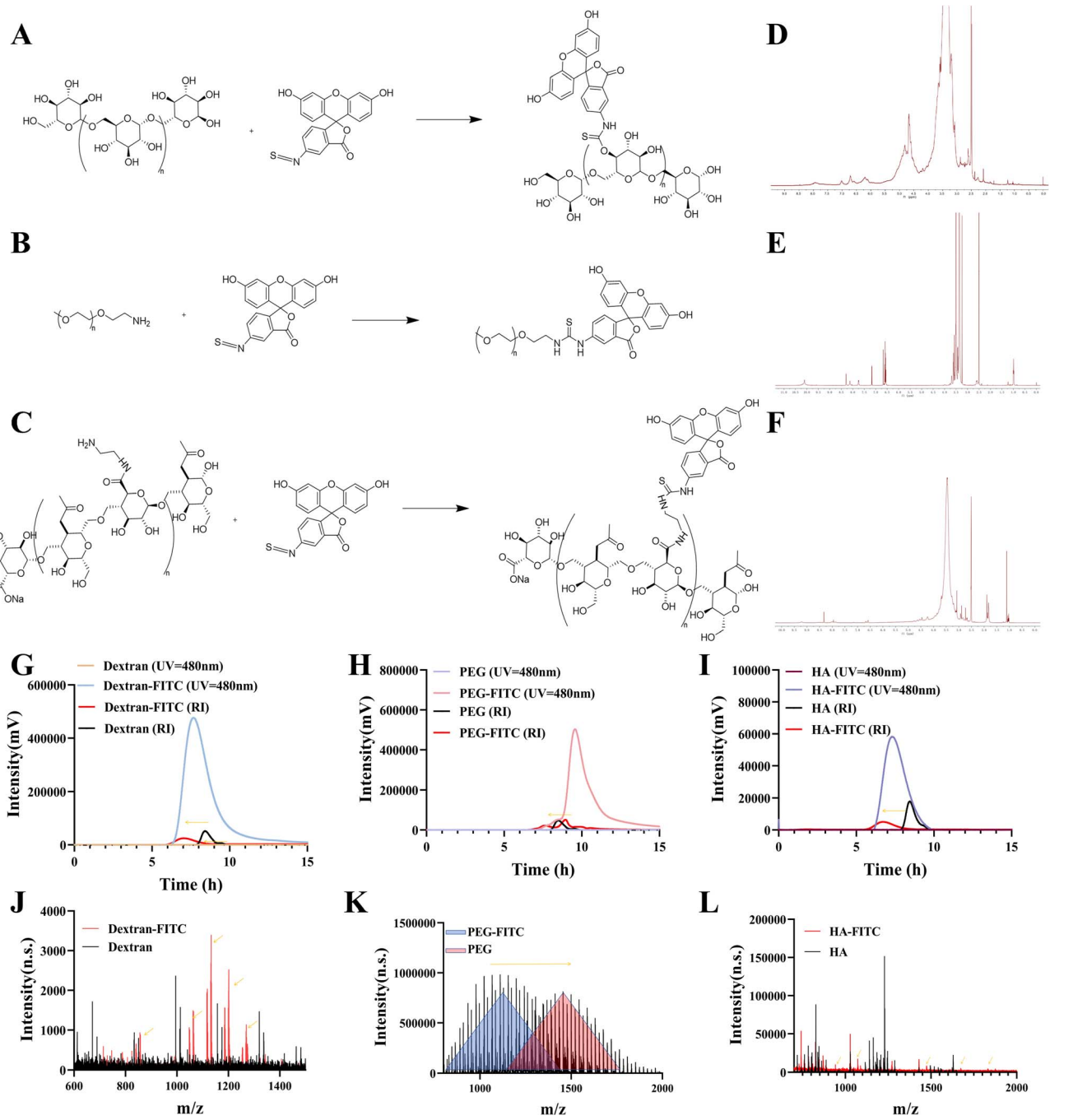

Fig. 1 (A) Dextran-FITC synthetic route; (B) PEG-FITC synthetic route; (C) HA-FITC synthetic route; (D) ^{1}H NMR of dextran-FITC; (E) ^{1}H NMR of PEG-FITC; (F) ^{1}H NMR of HA-FITC; (G) dextran and dextran-FITC GPC spectra; (H) PEG and PEG-FITC GPC spectra; (I) HA and HA-FITC GPC spectra; (J) dextran and dextran-FITC MALDI-TOF MS spectra; (K) PEG and PEG-FITC MALDI-TOF MS spectra; and (L) HA and HA-FITC MALDI-TOF MS spectra.

flasks containing high-glucose DMEM. Cells were incubated at 37 °C in a 5% CO_2 incubator, and cell attachment was observed 24 h post-revival. The medium was refreshed periodically, and cells were passaged upon reaching 80–90% confluence, ensuring healthy cell growth for subsequent experiments.

2.4.2 Cell viability assay. The CCK-8 assay was used to assess the cytotoxicity of various compounds on cell viability. Cells were seeded at 10 000 cells per well in a 96-well plate and incubated for 24 h at 37 °C in a 5% CO_2 environment. Following the removal of the medium, the cells were treated with media containing varying concentrations of dextran-FITC, PEG-FITC, and HA-FITC (1, 10, 100 μg mL^{-1} FITC eq.), along with a blank control (no probe) and a positive control (1% FITC in DMSO). After 24–48 h, 10 μL of CCK-8 solution was added to each well and incubated for 1–4 h, followed by absorbance measurement at 450 nm using a microplate reader. Cell viability

Open Access Article. Published on 19 August 2025. Downloaded on 5/22/2026 2:24:16 AM. This article is licensed under a Creative Commons Attribution-NonCommercial 3.0 Unported Licence.

was calculated based on the absorbance changes, and statistical analysis was performed to evaluate the cytotoxic effects of the probes.

2.4.3 Cellular uptake assay. PNAC-1 cells were cultured as a model to assess the internalization efficiency of the different probe delivery systems. Cells were maintained in DMEM containing 10% fetal bovine serum (FBS), 100 μg mL^{-1} streptomycin, and 100 μg mL^{-1} penicillin in a 5% CO_2 incubator at 37 °C. UV-sterilized (30 min exposure) dextran-FITC, PEG-FITC, and HA-FITC probes (10 μg mL^{-1} FITC eq.) were diluted in DMEM and added to cells cultured for 24 h to ensure cell adhesion. Cellular uptake was quantified using a microplate reader at designated time points.

2.4.4 Cell imaging assay. PNAC-1 cells were utilized as a model to evaluate the cellular uptake capabilities of the various probe delivery systems. Cells were cultured in DMEM supplemented with 10% FBS, 100 μg mL^{-1} streptomycin, and 100 μg mL^{-1} penicillin at 37 °C with 5% CO_2. Dextran-FITC, PEG-FITC, and HA-FITC (10 μg mL^{-1} FITC eq.) were dissolved under UV light and diluted in DMEM. After 4 h co-culture with PNAC-1 cells, the cells were washed three times with PBS buffer (10 mM, pH 7.4), fixed with 4% paraformaldehyde, and stained with DAPI (10 μg mL^{-1}) for nuclear visualization. Fluorescence microscopy was performed using an FITC filter set (Ex/Em = 488/520 nm).

2.5. 3D cell spheroid penetration assay

In the spheroid permeability assay, a 3D cellular spheroid model was established to evaluate the morphological changes and functional activity under varying osmotic conditions. Organoid spheroids were prepared in 96-well plates (7007, Corning, NY, USA) by seeding 1×10^5 cells per well, followed by centrifugation at 300×*g* for 5 min. Spheroids were cultured in DMEM supplemented with 2.5% Matrigel® matrix for 2 weeks, reaching an average diameter of 400–500 μm. These spheroids were divided into untreated and treated groups. Spheroid size was observed under an inverted microscope to ensure standardization. Probes (100 μg mL^{-1} FITC eq.) were added to the spheroids and incubated at 37 °C in a 5% CO_2 incubator for 24 h, with the untreated spheroids serving as controls. Probe penetration into the spheroids was observed by fluorescence microscopy, allowing the assessment of penetration efficiency and depth. Following probe treatment, the spheroids were thoroughly washed to remove residual probes in the medium. Fluorescence imaging was performed using a microscope (NIS, Nikon, Japan), and fluorescence intensity was quantified using the ImageJ software. Original RGB images were retained, and the red channel was extracted for analysis. Individual cell contours were manually outlined as regions of interest (ROI) using the "Freehand Selection" tool to measure the mean red channel fluorescence intensity (Mean Red Value). To correct background interference, at least three cell-free areas within the same image were selected to calculate the average background red fluorescence intensity, which was subtracted from the ROI measurements. All experiments were independently repeated three times to ensure data reliability.

2.6. *In vivo* probe distribution and tissue collection

In vivo experiments were conducted on 6 weeks-old Balb/c mice, with approval from the Animal Care and Welfare Committee of Guangxi Medical University (No.202405034). Tumor cells were mixed with Matrigel® in a 1 : 1 (v/v) ratio (1×10^6 PNAC-1 cells per mouse) and subcutaneously injected to establish xenograft models. Experimental interventions were initiated when the tumor volumes reached approximately 200 mm^3. The mice were maintained in a specific-pathogen-free (SPF) environment with a 12 h light–dark cycle, with food and water provided ad libitum. The biodistribution of the three materials was investigated by tail vein injection of 10 mg mL^{-1} FITC eq. probe solution (200 μL). IVIS analysis was performed at 2 h post-injection to monitor the accumulation and distribution of the probe in the tumor tissue. After sacrifice, the major organs and tumor tissues were harvested for biodistribution analysis. Approximately 0.1 g of tissue sample was homogenized with 1 mL of 0.9% sodium chloride (saline) using a cryogenic tissue grinder (pre-cooled to 4 °C) at 3000 rpm for 5 min. The homogenate was centrifuged at 12 000 rpm for 10 min at 4 °C. Subsequently, 200 μL of the supernatant was transferred to a 96-well plate, and the fluorescence intensity was measured using a microplate reader at Ex/Em = 488/520 nm to quantify the concentration of probe in the tissues.

2.7. Statistical analysis

To validate the assumption of homogeneity of variances between groups, an *F*-test was conducted before performing *t*-tests. If the *F*-test indicated no significant difference in standard deviation, a one-tailed, unpaired parametric *t*-test was used to compare the group means; otherwise, Welch's *t*-test was applied. Statistical analyses were conducted using GraphPad Prism (version 9.2.0), with a significance threshold set at $P < 0.05$.

3 Results and discussion

3.1. Synthesis of fluorescent materials

3.1.1 Optimized synthesis protocol for FITC-labeled polymers. Dextran-FITC was synthesized through the conjugation of FITC to dextran *via* its hydroxyl groups (Fig. 1A). The reaction proceeded in DMSO with the pH adjusted to 8.0 using $NaHCO_3$ under dark conditions with continuous stirring at room temperature (25 °C) for 24 h. Following purification and freeze-drying, structural confirmation was achieved by ^1H NMR (Fig. 1D). The characteristic dextran backbone signals (δ 3.0–5.2 ppm, 5H per glucopyranose unit) and FITC aromatic protons (δ 6.3–7.6 ppm, 9H) were integrated, indicating a modification ratio of approximately 1.11% (Fig. 1D and SI S1).

PEG-FITC was prepared *via* the covalent attachment of FITC to amine-terminated PEG (PEG-NH_2) in a water/DMSO solution (Fig. 1B). The mixture was stirred overnight at room temperature (25 °C). After centrifugation, purification, and freeze-drying, PEG-FITC was obtained. The ^1H NMR spectrum displays the characteristic PEG methylene resonances at δ 3.5 ppm (corresponding to 4H per $-OCH_2CH_2O-$ repeating

 © 2025 The Author(s). Published by the Royal Society of Chemistry

Open Access Article. Published on 19 August 2025. Downloaded on 5/22/2026 2:24:16 AM. This article is licensed under a Creative Commons Attribution-NonCommercial 3.0 Unported Licence.

unit) and FITC aromatic protons at δ 6.3–7.6 ppm (9H), with the modification ratio of approximately 1.02%, which was determined by integrating these characteristic peaks and calculating the ratio (Fig. 1E and SI S2).

The synthesis of HA-FITC involved coupling activated hyaluronic acid (HA) with FITC in water. The product was purified, and then freeze-dried (Fig. 1C). ^{1}H NMR analysis (D_2O, 400 MHz) confirmed the HA-FITC conjugation, where the characteristic hyaluronic acid backbone signals (δ 3.2–4.5 ppm, *N*-acetylglucosamine C1–C6 protons) and FITC aromatic protons (δ 6.3–7.6 ppm, 9H) were integrated, with the modification ratio of 0.42% (Fig. 1F and SI S3).

3.1.2 GPC, MALDI-TOF MS and spectroscopic analysis. UV-Vis spectra indicated the maximum absorption wavelength near 480 nm for dextran-FITC, PEG-FITC, and HA-FITC (SI S4). Given the negligible UV absorption at 480 nm for unmodified dextran, PEG, and HA at equivalent concentrations, this wavelength was selected as the monitoring parameter for the verification of conjugation (SI S4). As shown in Fig. 1G–I, the absorption intensity of the peak at 480 nm significantly increased for all the FITC-conjugated polymers compared to their unmodified counterparts, demonstrating their successful labeling. Furthermore, GPC analysis detected no residual free FITC, confirming the complete separation of the conjugated and unconjugated components through size-exclusion chromatography (Fig. 1G–I), respectively.

MALDI-TOF analysis revealed that dextran-FITC, PEG-FITC, and HA-FITC all exhibited molecular weight increments corresponding to multiples of 389 ($m/z = n \times M_{FITC}$). This finding was consistent with the refractive index (RI) detection results from GPC, confirming the successful conjugation of FITC to all three polymers (Fig. 1J–L), respectively. Fluorescence spectra identified characteristic excitation and emission maxima at approximately 480 nm and 520 nm (SI S4), respectively, for all the FITC-labeled polymers. Subsequent fluorescence measurements employed 480 nm excitation with detection at 520 nm emission. For quantitative comparisons, the samples were normalized to equivalent concentrations prior to measuring their fluorescence intensity at 480/520 nm.

3.1.3 Comparative analysis. After synthesizing the three materials, we found that the fluorescence absorption intensities of the three modified molecules were comparable at the same FITC eq. concentration, and the fluorescence intensities showed a gradient change with varying concentrations (SI S4). Therefore, subsequent experiments utilized a standardized concentration based on FITC equivalence (FITC eq.) to ensure consistent fluorescence intensity across all groups.

In our preliminary research, we discovered that high molecular weight polymers exhibit lower modification efficiency and encountered challenges in fabricating stable nanostructures. Consequently, the primary rationale for selecting low molecular weight PEG, HA, and dextran as the core polymeric carriers was their significant enhancement in tumor penetration efficiency of fluorescent probes. Firstly, low molecular weight PEG showed a superior performance in traversing tumor interstitial spaces. Research indicates that low molecular weight PEG chains can more effectively pass through the interstitial matrix to penetrate deep into tumors, thereby enhancing the delivery efficacy of the nanocarriers.[27] HA is particularly suitable for targeting cancer cells due to its high

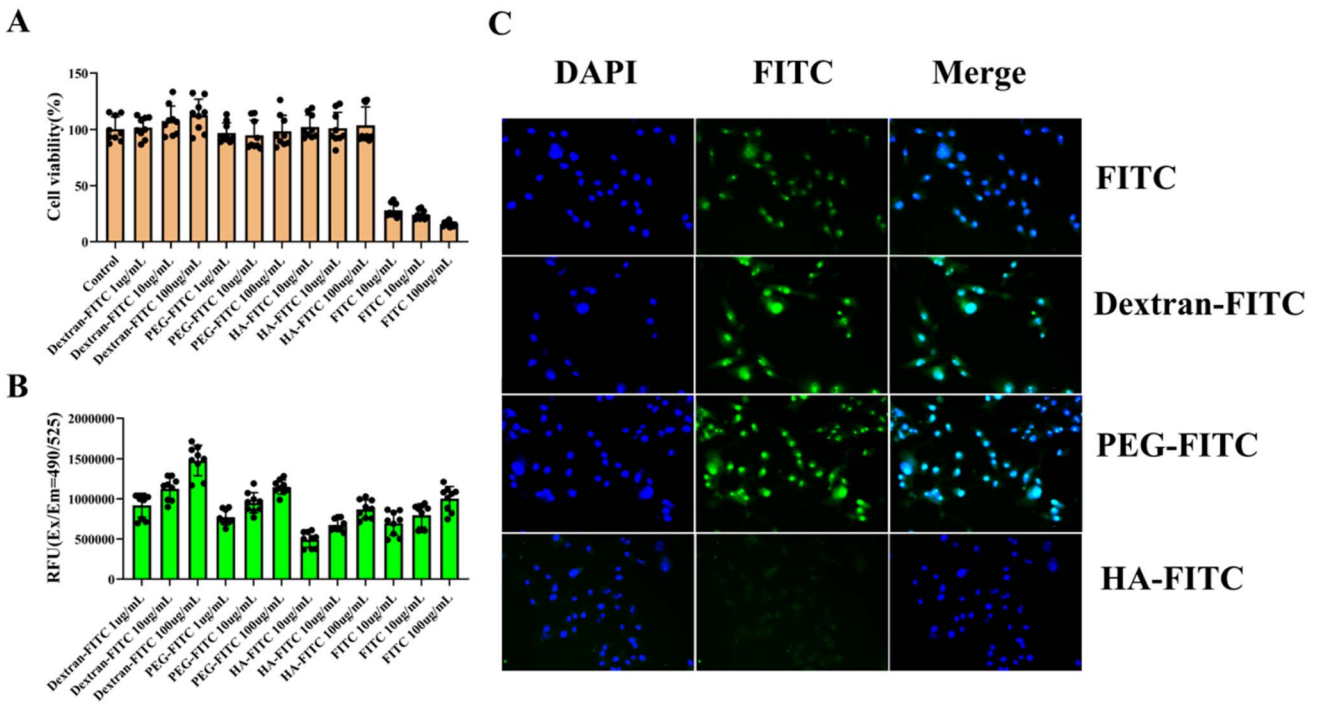

Fig. 2 (A) Cytotoxicity profiles of FITC-labeled polymeric conjugates and free FITC across three concentrations; (B) quantitative analysis of cellular uptake for FITC-conjugated polymers and free FITC at 1, 10, and 100 μg mL^{-1} eq. FITC; and (C) fluorescence microscopy visualization of polymer-FITC and free FITC internalization.

Open Access Article. Published on 19 August 2025. Downloaded on 5/22/2026 2:24:16 AM. This article is licensed under a Creative Commons Attribution-NonCommercial 3.0 Unported Licence.

affinity for CD44 receptors. Low molecular weight HA can effectively enter cells *via* CD44-mediated endocytosis, significantly enhancing the targeted delivery efficiency of probes.[28] Finally, low-molecular-weight dextran has higher endocytosis efficiency and fewer cellular uptake barriers compared to high molecular weight dextran, effectively improving the clarity and absorption efficiency of tumor imaging and tracking applications.[29] Therefore, the choice of low molecular weight PEG, HA, and dextran not only optimized the tumor penetration but also provided ideal polymer materials for tumor imaging.

3.2. Cytotoxicity and cellular uptake of FITC-labeled surgical navigation polymers

Cytotoxicity assessment represents a critical metric for evaluating the biocompatibility of fluorescent probes. Molecular enlargement *via* polymeric modification significantly reduces cytotoxicity, enhancing the biomedical utility of these probes.[30] Fig. 2A demonstrates the cytotoxicity profiles of dextran-FITC, PEG-FITC, and HA-FITC in PNAC-1 cells. Under FITC-equivalent concentrations of $\leq$100 μg mL^{-1}, no significant cytotoxicity was observed. In contrast, the small-molecule FITC exhibited statistically significant reductions in cell viability at concentrations as low as 1 μg mL^{-1}. In the meantime, dextran-FITC showed the strongest cellular uptake and fluorescence intensity, which was particularly evident in the cells under fluorescence microscopy, indicating its superior internalization efficiency (Fig. 2B). This is potentially due to the specific interactions between the dextran sugar molecules and the glycocalyx on the surface of tumor cells.[31] PEG-FITC also demonstrated significant cellular uptake (Fig. 2B), likely owing to its amphiphilic nature, where lipophilic moieties enhance the membrane penetration efficiency of polymeric systems.[32] Conversely, HA-FITC exhibited minimal cellular internalization due to its dependence on CD44 receptor-mediated endocytosis. However, the differential expression of CD44 limits the uptake efficiency through receptor specificity.[33] Furthermore, the strong negative charge of HA generates substantial electrostatic repulsion against the negatively charged cell membrane, further restricting non-receptor-mediated internalization.[34] Collectively, dextran-FITC demonstrated superior uptake efficiency in PNAC-1 cells, with prominent intracellular fluorescence signals. These properties underscore its potential as an intraoperative navigation material, characterized by effective tumor cell internalization and favorable tissue permeability. The superior intracellular transport efficiency of the HA/dextran/PEG-FITC conjugates relative to free FITC is visually confirmed in PANC-1 cells (Fig. 2C), corroborating the quantitative hierarchy of carrier-enhanced uptake shown in Fig. 2B (dextran-FITC > PEG-FITC > free FITC > HA-FITC). The differential intracellular distribution patterns of dextran-FITC, PEG-FITC, and HA-FITC demonstrate their differential cellular uptake and intracellular distribution patterns, reflecting polymer-specific variations in endocytic pathways and cell-binding affinities within PNAC-1 cells.

3.3. Comparative penetration in 3D tumor spheroids

Three-dimensional (3D) multicellular tumor spheroids (MCTS) serve as a physiologically relevant model for evaluating the penetration efficacy of a probe. Their dense extracellular matrix and cell–cell junctions mimic the diffusion barriers encountered in solid tumors, allowing quantitative assessment of the intratumoral transport kinetics. Fluorescence imaging combined with spatial intensity profiling in MCTS provides critical insights into the distribution patterns of the probe, where deeper penetration correlates with enhanced *in vivo* therapeutic potential. Fig. 3A illustrates the differential permeation of dextran-FITC, PEG-FITC, and HA-FITC in 3D PNAC-1 MCTS. Dextran-FITC exhibited the deepest penetration with the highest fluorescence intensity (Fig. 3B), demonstrating superior efficacy in complex tumor models. ImageJ-based quantification validated these results, supporting its potential for intraoperative navigation in deep-seated tumor tissues

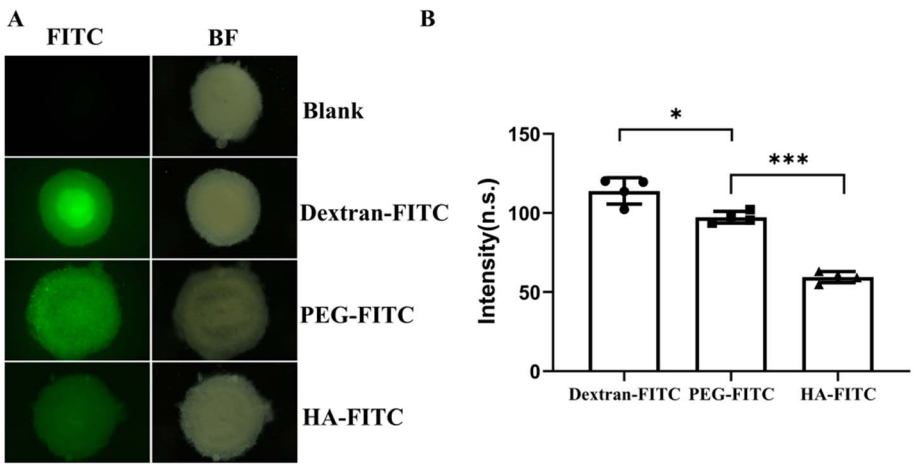

Fig. 3 (A) Intratumoral distribution profiles of fluorescent polymer conjugates in multicellular spheroids. (B) Quantitative fluorescence analysis *via* ImageJ: intensity and spatial penetration metrics. Data are presented as mean ± standard deviation (SD) from at least three independent experiments. One-way analysis of variance (ANOVA), followed by *post hoc* tests, was used for intergroup comparisons. Statistical significance is indicated as $*P < 0.05$ and $**P < 0.01$.

© 2025 The Author(s). Published by the Royal Society of Chemistry

Open Access Article. Published on 19 August 2025. Downloaded on 5/22/2026 2:24:16 AM.
This article is licensed under a Creative Commons Attribution-NonCommercial 3.0 Unported Licence.

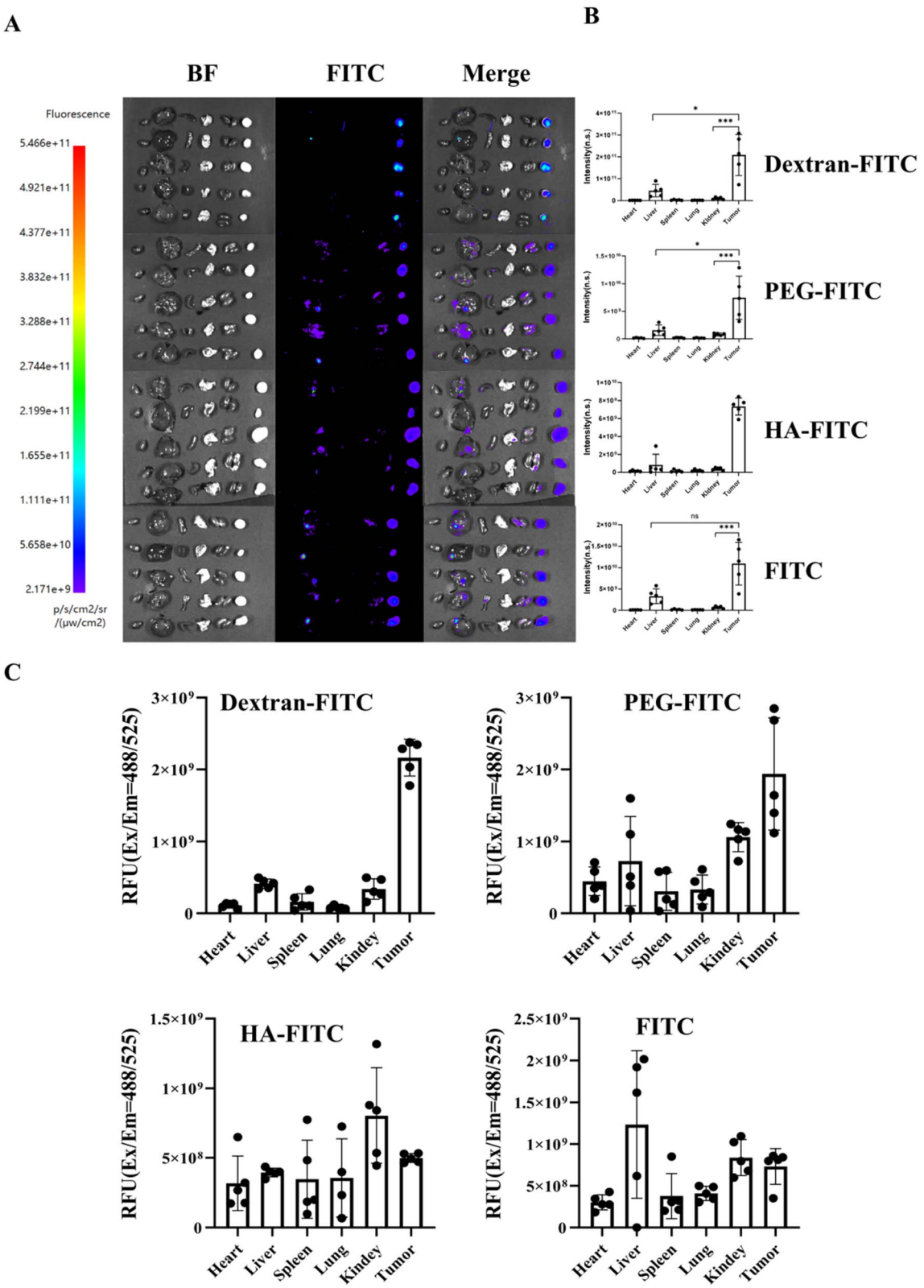

Fig. 4 (A) Representative bright-field, fluorescence, and merged images of murine heart, liver, spleen, lung, kidney, and tumor tissues 2 h post-administration of FITC-labeled compounds. (B) Quantitative analysis of fluorescence intensity in different organs and tumors. (C) Schematic workflow of fluorescence-based quantification of the probe concentration in murine tissues.

Open Access Article. Published on 19 August 2025. Downloaded on 5/22/2026 2:24:16 AM. This article is licensed under a Creative Commons Attribution-NonCommercial 3.0 Unported Licence.

(Fig. 3B). This enhanced penetration efficiency may be attributed to its smaller molecular weight and hydrophilicity,[35] enabling effective penetration through cell aggregates to label deeper cells. PEG-FITC exhibited moderate penetration with fluorescence predominantly localized at the spheroid periphery (Fig. 3A). This distribution pattern suggests its limited diffusion into deeper tumor regions. Conversely, HA-FITC displayed the weakest fluorescence signal and lowest permeability, which may due to its structural and receptor-binding constraints.

Beyond its hydrophilicity, the glycosyl properties of dextran-FITC likely represent the key factors for its deeper penetration capability in the three-dimensional model. This may be primarily attributed to its interactions with the abundant sugar molecules in the extracellular matrix (ECM) and on cell surfaces, a phenomenon discovered by MARI *et al.* in 2014.[19] The strong penetration of dextran-FITC in the 3D model indicates its effectiveness in navigating the complex tumor microenvironment, which is crucial for accurately marking deep tumor tissues during surgery. In contrast, the distribution of PEG-FITC was relatively shallow, possibly due to the structural characteristics of PEG, which despite having good biocompatibility, has a larger volume and spatial structure, creating steric hindrance that limits its penetration ability in tumor tissues.[36]

3.4. *In vivo* efficacy in tumor-targeting

The *in vivo* experiments confirm that dextran-FITC possesses superior tumor targeting (Fig. 4C), achieving the highest tumor fluorescence intensity, significantly exceeding that of PEG-FITC and HA-FITC, which indicates its enhanced tissue penetration and retention (Fig. 4A). Its fluorescence intensity increased post-injection (Fig. 4B), confirming its sustained tumor enrichment primarily *via* the passive targeting EPR effect (*i.e.*, enhanced tumor vascular permeability and impaired lymphatic drainage).[37] Regarding biodistribution, both dextran-FITC and PEG-FITC show high liver accumulation (indicating hepatic metabolism), while PEG-FITC exhibited the strongest renal signal (indicating predominant renal excretion). All the probes displayed weak signals in the lungs and heart, with that of dextran-FITC was slightly higher, suggesting its limited systemic distribution. HA-FITC showed the lowest fluorescence intensity in tumors and vital organs (no significant accumulation), potentially due to structural or metabolic constraints.[38] Comparatively, PEG/HA exhibited limitations, where the tumor signal of PEG-FITC decayed rapidly, reflecting its poor tumor retention and rapid clearance; although HA-FITC can distinguish tumors, its low penetration hinders detection (Fig. 4B and C), respectively. Notably, dextran-FITC displayed a significant liver/kidney distribution, necessitating long-term organ function studies and structural optimization to minimize its potential toxicity.

Overall, dextran emerged as the optimal tumor-targeted delivery platform due to its tumor-targeting mechanism, low cytotoxicity,[39,40] and tunable size that optimizes tumor extravasation, while minimizing renal clearance, which is critical for its sustained delivery.[41] Its hydrophilic polymer shield reduces its non-specific cellular uptake, enhancing its biocompatibility (validated by cytotoxicity tests) and metabolic stability (slow enzymatic degradation and dextranase resistance), which extends its systemic exposure.

4 Conclusion

This study systematically compared the tumor-targeted delivery efficiency of three polymer fluorescent probes, dextran-FITC, PEG-FITC, and HA-FITC, in pancreatic cancer. Using *in vivo* fluorescence imaging, we dynamically monitored and quantitatively evaluated their tumoral accumulation and systemic distribution. The results identified dextran-FITC as the most effective tumor-targeting delivery carrier among the three materials, exhibiting significantly higher tumor fluorescence intensity and accumulation capacity than PEG-FITC and HA-FITC. Dextran-FITC effectively penetrates deep tumor regions and enables efficient uptake by tumor cells, which were verified in 3D cell sphere models and *in vitro* experiments. Consequently, dextran-FITC has significant potential as an effective tumor-targeted probe with superior tumor-specific accumulation and retention properties, offering clinical value for applications including early tumor diagnosis (*e.g.*, intraoperative fluorescence navigation), drug delivery system development (to enhance chemotherapy/targeted drug concentrations at tumor sites), and real-time efficacy monitoring. Future research should focus on addressing its significant non-target distribution in the liver and kidney, aiming to reduce potential toxicity through structural optimization *via* molecular weight regulation or surface modification. This will accelerate its translation from basic research to clinical use as an efficient tumor-targeting vector.

Author contributions

Hongmian Jiang and Xiao Zhou developed the research design, evaluated all results and were responsible for the article. Xiao Zhou and Huang Huanli developed the experimental design and analysed the data. Xiao Zhou, Huangli Huang, Lifeng Luo and Chenxi Cui performed research and contributed to the writing of this paper.

Conflicts of interest

The authors declare that there are no conflicts of interest.

Data availability

The data used in this study can be requested *via* the email of the corresponding author. Requesters are required to provide relevant information to facilitate the verification and processing of the access request. We encourage interested researchers to contact us for data access, ensuring compliance with applicable ethical and legal regulations.

The SI file contains experimental procedures, characterization data (NMR, GLC, MALDI TOF MS), and supporting figures/tables not included in the main text. See DOI: **https://doi.org/10.1039/d5ra02236c**.

© 2025 The Author(s). Published by the Royal Society of Chemistry

Open Access Article. Published on 19 August 2025. Downloaded on 5/22/2026 2:24:16 AM. This article is licensed under a Creative Commons Attribution-NonCommercial 3.0 Unported Licence.

Acknowledgements

This work was supported by the self-funded research project of the Health Commission of Guangxi Zhuang Autonomous Region (Grant No. Z-A20231144 and Z-A20240991), the self-funded research project of Administration of Traditional Chinese Medicine of Guangxi Zhuang Autonomous Region (Grant No. GXZYA20240466), project of Scientific Research and Technological Development Program of Nanning (20253036-2), and the Key Clinical Specialist Pathology Unit Program of Guangxi Zhuang Autonomous Region (2023QZD01).

References

1 R. L. Siegel, K. D. Miller and A. Jemal, Cancer statistics, 2019, *Ca-Cancer J. Clin.*, 2019, **69**(1), 7–34.
2 M. Pal, T. Muinao, H. P. D. Boruah and N. Mahindroo, Current advances in prognostic and diagnostic biomarkers for solid cancers: Detection techniques and future challenges, *Biomed. Pharmacother.*, 2022, **146**, 112488.
3 E. N. D. Kok, R. Eppenga, K. F. D. Kuhlmann, H. C. Groen, R. van Veen, J. M. van Dieren, T. R. de Wijkerslooth, M. van Leerdam, D. M. J. Lambregts, W. J. Heerink, N. J. Hoetjes, O. Ivashchenko, G. L. Beets, A. G. J. Aalbers, J. Nijkamp and T. J. M. Ruers, Accurate surgical navigation with real-time tumor tracking in cancer surgery, *npj Precis. Oncol.*, 2020, **4**, 8.
4 H. Han and H. Chen, Selective lymph node dissection in early-stage non-small cell lung cancer, *J. Thorac. Dis.*, 2017, **9**(7), 2102–2107.
5 J. Ahmed, C. Torrado, A. Chelariu, S. H. Kim and J. R. Ahnert, Fusion Challenges in Solid Tumors: Shaping the Landscape of Cancer Care in Precision Medicine, *JCO Precis. Oncol.*, 2024, **8**, e2400038.
6 S. B. Hong, S. S. Lee, J. H. Kim, H. J. Kim, J. H. Byun, S. M. Hong, K.-B. Song and S. C. Kim, Pancreatic Cancer CT: Prediction of Resectability according to NCCN Criteria, *Radiology*, 2018, **289**(3), 710–718.
7 A. Moore and T. Donahue, Pancreatic Cancer, *JAMA*, 2019, **322**(14), 1426.
8 M. Schneider, T. Hackert, O. Strobel and M. W. Büchler, Technical advances in surgery for pancreatic cancer, *Br. J. Surg.*, 2021, **108**(7), 777–785.
9 S. Boeck and V. Heinemann, Improving post-surgical management of resected pancreatic cancer, *Lancet*, 2017, **390**(10097), 847–848.
10 L. Su, X. Zhu, H. Ding, L. Hu, J. Chen, S. Qi, K. Luo, W. Ling and X. Tian, Intraoperative tumor mapping using pyridine-carbazole based multifunctional fluorescent probes for precise resection and photodynamic therapeutics, *Sens. Actuators, B*, 2024, **412**, 135792.
11 T. Opacic, S. Dencks, B. Theek, M. Piepenbrock, D. Ackermann, A. Rix, T. Lammers, E. Stickeler, S. Delorme, G. Schmitz and F. Kiessling, Motion model ultrasound localization microscopy for preclinical and clinical multiparametric tumor characterization, *Nat. Commun.*, 2018, **9**(1), 1527.
12 A. S. Naidu, M. D. Naish and R. V. Patel, A Breakthrough in Tumor Localization: Combining Tactile Sensing and Ultrasound to Improve Tumor Localization in Robotics-Assisted Minimally Invasive Surgery, *IEEE Robot. Autom. Mag.*, 2017, **24**(2), 54–62.
13 K. Wang, Y. Du, Z. Zhang, K. He, Z. Cheng, L. Yin, D. Dong, C. Li, W. Li, Z. Hu, C. Zhang, H. Hui, C. Chi and J. Tian, Fluorescence image-guided tumour surgery, *Nat. Rev. Bioeng.*, 2023, **1**(3), 161–179.
14 S. Hernot, L. van Manen, P. Debie, J. S. D. Mieog and A. L. Vahrmeijer, Latest developments in molecular tracers for fluorescence image-guided cancer surgery, *Lancet Oncol.*, 2019, **20**(7), e354–e367.
15 Q. Guo and C. Jiang, Delivery strategies for macromolecular drugs in cancer therapy, *Acta Pharm. Sin. B*, 2020, **10**(6), 979–986.
16 H. Wang, X. Ji, Z. Li and F. Huang, Fluorescent Supramolecular Polymeric Materials, *Adv. Mater.*, 2017, **29**(14), 1606117.
17 H. Chen, D. Liu, Y. Li, X. Xu, J. Xu, N. N. Yadav, S. Zhou, P. C. M. van Zijl and G. Liu, CEST MRI monitoring of tumor response to vascular disrupting therapy using high molecular weight dextrans, *Magn. Reson. Med.*, 2019, **82**(4), 1471–1479.
18 P. Bitsch, E. S. Baum, I. Beltrán Hernández, S. Bitsch, J. Harwood, S. Oliveira and H. Kolmar, Penetration of Nanobody-Dextran Polymer Conjugates through Tumor Spheroids, *Pharmaceutics*, 2023, **15**(10), 2374.
19 S. M. Sagnella, H. Duong, A. MacMillan, C. Boyer, R. Whan, J. A. McCarroll, T. P. Davis and M. Kavallaris, Dextran-based doxorubicin nanocarriers with improved tumor penetration, *Biomacromolecules*, 2014, **15**(1), 262–275.
20 S. S. Guan, C. T. Wu, C. Y. Chiu, T. Y. Luo, J. Y. Wu, T. Z. Liao and S. H. Liu, Polyethylene glycol-conjugated HER2-targeted peptides as a nuclear imaging probe for HER2-overexpressed gastric cancer detection in vivo, *J. Transl. Med.*, 2018, **16**(1), 168.
21 W.-L. Cui, M.-H. Wang, Y.-H. Yang, J. Qu, H. Zhang, X. Zhu and J.-Y. Wang, A water-soluble polymer fluorescent probe *via* RAFT polymerization for dynamic monitoring of cellular lipid droplet levels and zebrafish imaging, *New J. Chem.*, 2022, **46**(34), 16539–16546.
22 J. Gao, Y. Wang, R. Wang, M. Liu, H. Wang, J. Li and J. Du, Preclinical studies of a PARP-targeted theranostic radiopharmaceutical for pancreatic cancer, *Front. Pharmacol*, 2025, **16**, 1576587.
23 D. Bhattacharya, D. Svechkarev, J. J. Souchek, T. K. Hill, M. A. Taylor, A. Natarajan and A. M. Mohs, Impact of structurally modifying hyaluronic acid on CD44 interaction, *J. Mater. Chem. B*, 2017, **5**(41), 8183–8192.
24 T. Koltai, S. J. Reshkin, T. M. A. Carvalho and R. A. Cardone, Targeting the Stromal Pro-Tumoral Hyaluronan-CD44 Pathway in Pancreatic Cancer, *Int. J. Mol. Sci.*, 2021, **22**(8), 3953.
25 J. Zhu, L. Xu, W. Wang, M. Xiao, J. Li, L. Wang and X. Jiang, Molecular Dynamics Simulations Reveal Octanoylated

Open Access Article. Published on 19 August 2025. Downloaded on 5/22/2026 2:24:16 AM. This article is licensed under a Creative Commons Attribution-NonCommercial 3.0 Unported Licence.

Hyaluronic Acid Enhances Liposome Stability, Stealth and Targeting, *ACS Omega*, 2024, **9**(31), 33833–33844.

26 A. E. Caprifico, E. Polycarpou, P. J. S. Foot and G. Calabrese, Biomedical and Pharmacological Uses of Fluorescein Isothiocyanate Chitosan-Based Nanocarriers, *Macromol. Biosci.*, 2021, **21**(1), e2000312.

27 F. M. Veronese and G. Pasut, PEGylation, successful approach to drug delivery, *Drug Discovery Today*, 2005, **10**(21), 1451–1458.

28 C. He, J. Zhou, X. Wu, Y. Zhou, S. Wang, B. Liu, T. Luo, Y. Chen, J. Yuan, D. Wang, C. Zhang and J. Shi, Hyaluronic acid-zein shell-core biopolymer nanoparticles enhance hepatocellular carcinoma therapy of celastrol *via* CD44-mediated cellular uptake, *Int. J. Biol. Macromol.*, 2024, **281**(Pt 1), 136096.

29 G. Liu, S. R. Banerjee, X. Yang, N. Yadav, A. Lisok, A. Jablonska, J. Xu, Y. Li, M. G. Pomper and P. van Zijl, A dextran-based probe for the targeted magnetic resonance imaging of tumours expressing prostate-specific membrane antigen, *Nat. Biomed. Eng.*, 2017, **1**, 977–982.

30 Z. Wang, J. Ma, C. Li and H. Zhang, Conjugated Aggregation-Induced Fluorescent Materials for Biofluorescent Probes: A Review, *Biosensors*, 2023, **13**(2), 159.

31 A. Buffone and V. M. Weaver, Don't sugarcoat it: How glycocalyx composition influences cancer progression, *J. Cell Biol.*, 2020, **219**(1), e201910070.

32 K. Kanazaki, K. Sano, A. Makino, F. Yamauchi, A. Takahashi, T. Homma, M. Ono and H. Saji, Feasibility of poly(ethylene glycol) derivatives as diagnostic drug carriers for tumor imaging, *J. Controlled Release*, 2016, **226**, 115–123.

33 V. Abetamann, H. F. Kern and H. P. Elsässer, Differential expression of the hyaluronan receptors CD44 and RHAMM in human pancreatic cancer cells, *Clin. Cancer Res.*, 1996, **2**(9), 1607–1618.

34 K. M. Sahu, S. Patra and S. K. Swain, Host–guest drug delivery by β-cyclodextrin assisted polysaccharide vehicles: A review, *Int. J. Biol. Macromol.*, 2023, **240**, 124338.

35 Z. Han, C. Chen, X. Xu, R. Bai, V. Staedtke, J. Huang, K. W. Y. Chan, J. Xu, D. O. Kamson, Z. Wen, L. Knutsson, P. C. M. van Zijl and G. Liu, Dynamic contrast-enhanced CEST MRI using a low molecular weight dextran, *NMR Biomed.*, 2022, **35**(3), e4649.

36 D. Lainšček, A. Golob-Urbanc and S. Orehek, In Vivo Bioluminescence and Fluorescence Imaging: Optical Tool for Cancer Research, in M. Čemažar, T. Jesenko and U. Lampreht Tratar ed. *Mouse Models of Cancer: Methods and Protocols*, Springer US, New York, NY, 2024, pp. 105–123.

37 R. Sun, J. Xiang, Q. Zhou, Y. Piao, J. Tang, S. Shao, Z. Zhou, Y. H. Bae and Y. Shen, The tumor EPR effect for cancer drug delivery: Current status, limitations, and alternatives, *Adv. Drug Delivery Rev.*, 2022, **191**, 114614.

38 Z. Luo, Y. Dai and H. Gao, Development and application of hyaluronic acid in tumor targeting drug delivery, *Acta Pharm. Sin. B*, 2019, **9**(6), 1099–1112.

39 Z. Han, S. Zhang, K. Fujiwara, J. Zhang, Y. Li, J. Liu, P. C. M. van Zijl, Z. R. Lu, L. Zheng and G. Liu, Extradomain-B Fibronectin-Targeted Dextran-Based Chemical Exchange Saturation Transfer Magnetic Resonance Imaging Probe for Detecting Pancreatic Cancer, *Bioconjugate Chem.*, 2019, **30**(5), 1425–1433.

40 B. J. Bie, X. R. Zhao, J. R. Yan, X. J. Ke, F. Liu and G. P. Yan, Dextran Fluorescent Probes Containing Sulfadiazine and Rhodamine B Groups, *Molecules*, 2022, **27**(19), 6747.

41 E. M. Higbee-Dempsey, A. Amirshaghaghi, M. J. Case, M. Bouché, J. Kim, D. P. Cormode and A. Tsourkas, Biodegradable Gold Nanoclusters with Improved Excretion Due to pH-Triggered Hydrophobic-to-Hydrophilic Transition, *J. Am. Chem. Soc.*, 2020, **142**(17), 7783–7794.

© 2025 The Author(s). Published by the Royal Society of Chemistry